Comput Mech (2016) 58:391–409
DOI 10.1007/s00466-016-1299-6

ORIGINAL PAPER

A meshfree continuous–discontinuous approach for the ductile fracture modeling in explicit dynamics analysis

C. T. Wu[1] · N. Ma[2] · K. Takada[3] · H. Okada[3]

Received: 3 February 2016 / Accepted: 3 May 2016 / Published online: 20 May 2016

Abstract This paper presents a combined continuous–discontinuous modeling technique for the dynamic ductile fracture analysis using an interactive particle enrichment algorithm and a strain-morphed nonlocal meshfree method. The strain-morphed nonlocal meshfree method is a nodel-integrated meshfree method which was recently proposed for the analysis of elastic-damage induced strain localization problems. In this paper, the strain-morphed nonlocal meshfree formulation is extended to the elastic–plastic-damage materials for the ductile fracture analysis. When the ductile material is fully degraded, the interactive particle enrichment scheme is introduced in the strain-morphed nonlocal meshfree formulation that permits a continuous-to-discontinuous failure modeling. The essence of the interactive particle enrichment algorithm is a particle insertion–deletion scheme that produces a visibility criterion for the description of a traction-free crack and leads to a better presentation of the ductile fracture process. Several numerical benchmarks are examined using the explicit dynamics analysis to demonstrate the effectiveness and accuracy of the proposed method.

Keywords Meshfree · Nodal integration · Nonlocal · Stabilization · Regularization

✉ C. T. Wu
ctwu@lstc.com

[1] Livermore Software Technology Corporation (LSTC), Livermore, CA 94551, USA

[2] Engineering Technology Division, JSOL Corporation, Osaka 550-0001, Japan

[3] Automobile R&D Center, Honda R&D Co., Ltd, Tochigi 321-3393, Japan

1 Introduction

While modern multiscale and multiresolution techniques are able to [1–4] offer reproduction and estimation of some complex phenomena of ductile fracture in metals, the development of an efficient and easy-to-use approach for macroscopic modeling is also very important for many large-scale industrial applications. In macroscopic analysis, continuum damage models [5,6] are often considered effective to describe the degradation of materials as a consequence of the growth of microstructural defects such as micro-voids and micro-cracks. Mathematically the strain-softening in the local form of continuum damage model leads to the ill-posed boundary value problem [7,8], and the numerical results suffer from the pathological localization of deformation. Several integral-type and gradient-type of nonlocal damage models [9,10] were developed for finite element methods to regularize the non-unique solution and minimize the mesh dependence in strain localization problem. The numerical methods utilizing those nonlocal damage models are known to best suit for modeling diffuse micro-cracking and formation of the damage zone before a macro-crack is evident. When the coalescence of some microstructural defects creates the macro-crack, the discrete fracture becomes dominant in which fracture is regarded as the ultimate consequence of the material degradation process [6]. Unfortunately, the numerical methods based on a pure nonlocal damage model are inadequate to describe such kinematic discontinuity of the displacement field in a continuous setting. Without introducing an explicit failure surface to the numerical model, excessive straining arises since the material across the damage zone remains kinematically connected at almost zero stress levels [11,12]. As a consequence, a spurious damage growth [13,14] is often observed in the numerical solution which strongly disagrees with the physical observation.

The incorporation of a discontinuity in the displacement field has shown to be the necessity to release the excessive strain in the damage zone generated by the nonlocal damage model employed on various numerical methods. This has motivated the development of various *combined continuous–discontinuous approaches* [11,14–17] to model the entire fracture process, from material degradation to crack propagation in ductile as well as in brittle materials. While the nonlocal damage model is used to describe the material degradation, the discontinuous enrichment [18–20] and remeshing technique [11] typically used in fracture mechanics are considered to model the discrete crack. The transition from continuous model to discontinuous model is an irreversible process. This transition process can be made either at partial or complete local failure of the continuous material. In the case of partial local failure, the relationship between the damage zone and the macro-crack is made thermodynamically [15,17,18] such that the energy dissipated due to the damage is equivalent to the energy required to establish the crack surface. In the complete local failure case, the transition from damage to crack is triggered when the material is fully degraded. In other words, a traction-free crack [11,21] is introduced to the numerical model as the damage variable is close to one. Recent years, more sophisticated and accurate simulations have been made within the finite element framework for the combined continuous–discontinuous failure analysis in the brittle [12,22,23] and ductile [24,25] materials.

Compare with finite element methods, considerable success also has been achieved in meshfree methods for damage and fracture analyses. Simonsen and Li [26] first proposed a meshfree simulation of crack growth in ductile materials. In their method, the reproducing kernel (RK) approximation [27] is utilized to approximate the displacement field which contains the cracks modelled by the visibility method [28]. The method has been applied to the analysis of ductile fracture in thermal–mechanical [29], high-speed [30] and structural [31] problems. On the other hand, meshfree methods utilizing continuous damage model experience the pathological localization problem [32] in deformation similar to that in standard finite element methods. Several meshfree regularization techniques have been developed to overcome this numerical obstacle in modeling the material damage using the continuous approach. Based on the concept of nonlocal damage modeling techniques [9,10,33] and RK approximation [27], Chen et al. [34] developed a meshfree strain smoothing procedure to remedy the discretization sensitivity in damage-induced strain localization problem. The relationship between the meshfree integral-type and gradient-type of nonlocal damage models [35] at the discrete level was established under their meshfree regularization framework [34]. Subsequently, the meshfree regularization procedure was applied to the stabilized conforming nodal integration (SCNI) method [36] leading to a nodal-integrated smoothed strain field [37] for strain localization problem. Both elastic-damage analysis [37] and elasto-plastic damage analysis [38] have been conducted using this nodal-integrated regularized meshfree method in explicit dynamics simulation. Nevertheless, an implementation of those meshfree regularization procedures still relies on the background integration cells which pose substantial numerical challenges to model the discrete cracks in combined continuous–discontinuous approach.

On the other hand, the characteristics of discretization flexibility and customized approximation have made meshfree methods favorable [28] for modeling the discrete cracks in brittle fracture analysis. The discontinuous approach in meshfree methods describes the discontinuity of displacement field by either the modification of kernel (weight) function or the enrichment of discontinuous function. The representatives of the first technique include the visibility method [28], diffraction method [39], transparency method [39] and other improved methods based on geometric information and different screening effects [40,41]. Among them, the visibility method is considered the earliest and easiest approach to model the propagation of arbitrary cracks [42]. The second technique incorporates the enrichment functions with meshfree approximations either intrinsically or extrinsically [43–45] to describe the discontinuous and singular fields of the crack problem. Regardless the ability to avoid complex remeshing operations and to minimize the sensitivity of mesh alignment, meshfree methods based on the background integration cells make them difficult to integrate the strain regularization techniques with meshfree discontinuous approaches for the ductile fracture analysis. In principle, this demands the development of a nodal-integrated meshfree framework for the combined continuous–discontinuous approach.

Meshfree methods based on a direct nodal integration scheme exhibit poor performance [46] in modeling solid mechanics problems. This poor performance is well-known as the spurious deformation modes caused by rank instability of the meshfree discrete system [47]. A pioneering approach to circumvent this numerical instability using stabilization procedure was demonstrated by Beissel and Belytschko [48]. This stabilization method reconstructs the Galerkin weak form consisting of the residual of equilibrium equation to stabilize the solution. The stabilized meshfree method [47] is closely related to the Galerkin/Least-Squares (GLS) method [49] and the Galerkin methods equipped with bubble functions [50]. Nevertheless, the main drawback of this residual stabilization approach is the contradictory demands on the stabilization control parameter placed by accuracy requirement. The SCNI [36] method is a meshfree nodal integration method that bypasses the need of stabilization control parameter. The central to this method is the "integra-

tion constraint" in which a strain-smoothing algorithm was developed to meet this integration constraint and served as a stabilization process for meshfree nodal integration. Over the past decade, the SCNI scheme has undergone extensive developments [51,52] and led to widespread meshfree applications [38] in engineering. A recent meshfree stabilization method is the approach based on the strain gradient stabilization (SGS) scheme [53,54]. The idea is to use a second-order penalty term derived based on the decomposed strain field from the meshfree displacement smoothing [55,56] as a means of stabilizing the meshfree method. While the SCNI scheme uses single stress point per node for the background cell integration, the SGS scheme uses dual stress points [57] at each node for the direct nodal integration. With the SGS scheme, a strain-morphed nonlocal meshfree method [58] was recently presented to couple the locality and non-locality of the decomposed strain field for the stabilized and regularized analyses of elastic-damage induced strain localization problem. A unique property of the resultant strain-morphed nonlocal meshfree formulation is it does not require the background cells for the domain integration.

The main goal of this paper is to develop a combined meshfree continuous–discontinuous technique that supports arbitrary crack initiation and propagation in ductile fracture simulation, while avoiding many of the stability problems in traditional meshfree techniques. This new modeling technique concerns the strain-morphed nonlocal meshfree method that models the degradation of ductile materials and an interactive particle enrichment algorithm that describes the formation of macro-cracks. The rest of the paper is organized as follows. In the next section, the strain-morphed nonlocal meshfree method is reviewed in the context of continuum damage mechanics for dynamic problems. In Sect. 3, an interactive particle enrichment algorithm for crack initiation and propagation is introduced. The corresponding variational formulation and discrete equations are given in Sect. 4. Three numerical examples are presented in Sect. 5 to illustrate the robustness and accuracy of the proposed method. Section 6 concludes with a brief summary.

2 The strain-morphed nonlocal meshfree method

Consider a two-dimensional body Ω^0 containing an initial crack Γ_f^0 which is defined in the reference configuration as shown in Fig. 1. The image of $\Omega^0$is the current domain denoted by Ω, and the motion Φ is described by $\boldsymbol{x} = \Phi(\boldsymbol{X}, t)$, where $t \in [0, T]$ is the time, $\boldsymbol{X}$ and $\boldsymbol{x}$ are material and spatial coordinates, respectively. The strong form of the dynamic problem can be stated by the following [59,60]:

$$\sigma_{ij,j} + \rho b_i = \rho \ddot{u}_i \quad in \quad \Omega \tag{1}$$

$$u_i = g_i \quad on \quad \Gamma_g \tag{2}$$

$$\sigma_{ij} n_j = h_i \quad on \quad \Gamma_h \tag{3}$$

$$\sigma_{ij} n_j = t_i^c \left([[u_i]]\right) \quad on \quad \Gamma_f \tag{4}$$

where σ_{ij} is the Cauchy stress tensor, ρ is material density, b_i is the component of body force, u_i is the displacement component, g_i is the prescribed boundary displacement, n_i is the unit outward normal vector, h_i is the traction imposed on Neumann boundary, and t_i^c is cohesive traction applied on the discontinuity line Γ_f. Notation $[[\boldsymbol{u}]]$ represents the displacement jump across the discontinuity line Γ_f . Within the framework of continuum damage mechanics, we can decompose the problem domain into two non-overlapping zones, an undamaged zone Ω_b and a damage zone Ω_c, as follows:

$$\bar{\Omega} = \bar{\Omega}_b \cup \bar{\Omega}_c \tag{5}$$

$$\Gamma_d = \bar{\Omega}_b \cap \bar{\Omega}_c \tag{6}$$

$$\Omega_b = \{\boldsymbol{x} \in \Omega \,|d\,(\boldsymbol{x}) = 0\} \subset \Omega \tag{7}$$

$$\Omega_c = \{\boldsymbol{x} \in \Omega \,|0 < d\,(\boldsymbol{x}) < 1\} \subset \Omega \tag{8}$$

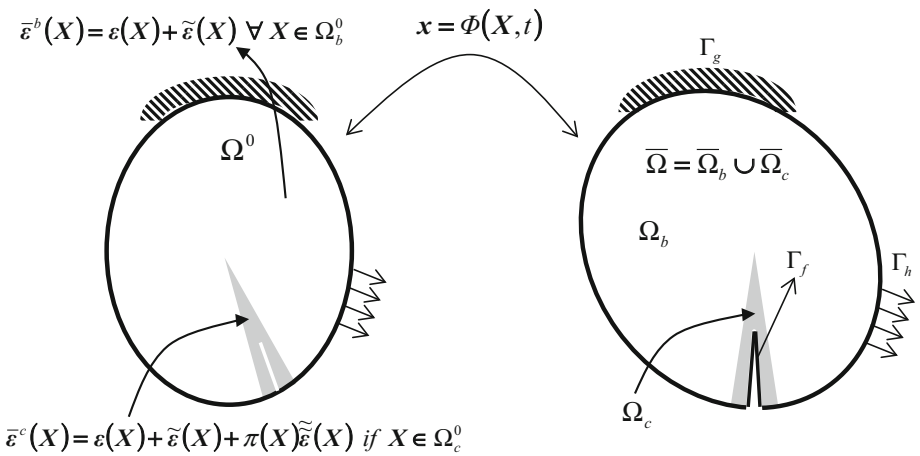

Fig. 1 The strain-morphed nonlocal meshfree model for local and non-local strain approximations

where $d(\boldsymbol{x}) \in [0, 1]$ is a scalar that stands for the damage variable in the isotropic continuum damage model [5,6]. We note that the discontinuity line Γ_f is a moving interface which travels with the evolution of monotone non-decreasing damage d. We also note that $\partial\Omega = \Gamma_g \cup \Gamma_h \cup \Gamma_f$, $\Gamma_g \cap \partial\Gamma_f = \varnothing$ and $\Gamma_h \cap \partial\Gamma_f = \varnothing$.

Without the consideration of discontinuous approach for the crack propagation problem, we have to limit the damage variable to be bonded by $d < 1$ for the weak-discontinuity approach such that the fully damage ($d = 1$) does not occur. Under this condition, the strain field in the strain-morphed nonlocal meshfree method [58] can be established by coupling the decomposed strain fields from a meshfree strain smoothing technique [58] in the following form

$$\bar{\boldsymbol{\varepsilon}}(\boldsymbol{x}) = \begin{cases} \bar{\boldsymbol{\varepsilon}}^b(\boldsymbol{x}) = \boldsymbol{\varepsilon}(\boldsymbol{x}) + \tilde{\boldsymbol{\varepsilon}}(\boldsymbol{x}) & \forall \boldsymbol{x} \in \Omega_b \\ \bar{\boldsymbol{\varepsilon}}^c(\boldsymbol{x}) = \boldsymbol{\varepsilon}(\boldsymbol{x}) + \tilde{\boldsymbol{\varepsilon}}(\boldsymbol{x}) + \pi(\boldsymbol{x})\,\tilde{\tilde{\boldsymbol{\varepsilon}}}(\boldsymbol{x}) & \forall \boldsymbol{x} \in \Omega_c \end{cases} \tag{9}$$

where $\boldsymbol{\varepsilon}(\boldsymbol{x})$ is the nodal value of local strain field approximated by the standard meshfree shape functions. The decomposed strain field $\tilde{\boldsymbol{\varepsilon}}$ contains the first-order strain gradient term for stabilization and is defined by [58]

$$\tilde{\boldsymbol{\varepsilon}} = \nabla\boldsymbol{\varepsilon}(\boldsymbol{x}) \cdot \boldsymbol{\lambda}^b(\boldsymbol{x}) \tag{10}$$

$$\boldsymbol{\lambda}^b(\boldsymbol{x}) = \int_\Omega \tilde{\Psi}^b(\boldsymbol{x}; \boldsymbol{x} - \boldsymbol{\xi})(\boldsymbol{\xi} - \boldsymbol{x})\, d\Omega \tag{11}$$

where $\tilde{\Psi}^b$ is the strain smoothing function for stabilization in meshfree nodal integration method, $\tilde{\Psi}^b(\boldsymbol{r}) > 0$ for $\|\boldsymbol{r}\| < b$, $\tilde{\Psi}^b(\boldsymbol{r}) = 0$ for $\|\boldsymbol{r}\| \geq b$, and subscript b denotes the radius of influence domain for the strain smoothing function. Another decomposed strain field $\tilde{\tilde{\boldsymbol{\varepsilon}}}$ is a non-local strain field that contains the second-order strain gradient term for regularization and is defined by [58]

$$\tilde{\tilde{\boldsymbol{\varepsilon}}}(\boldsymbol{x}) = \nabla^{(2)}\boldsymbol{\varepsilon}(\boldsymbol{x}) \cdot^{(2)} \boldsymbol{\eta}^c(\boldsymbol{x}) \tag{12}$$

$$\boldsymbol{\eta}^c(\boldsymbol{x}) = \frac{1}{2!}\int_\Omega \tilde{\Psi}^c(\boldsymbol{x}; \boldsymbol{x} - \boldsymbol{\xi})(\boldsymbol{\xi} - \boldsymbol{x})^{(2)}\, d\Omega \tag{13}$$

where $\nabla^{(2)}$ denotes the 2nd order gradient operator and $\cdot^{(2)}$ denotes the 2nd order inner product. Analogously, $\tilde{\Psi}^c$ is the strain smoothing function for regularization in meshfree nodal integration method. The radius size c of $\tilde{\Psi}^c(\mathbf{x})$ is a material length parameter which can be related to the scale of the microstructure [33] in damage-induced strain localization problem. A simple choice of morphing function $\pi(\boldsymbol{x})$ in Eq. (9) is given by [58]

$$\pi(\boldsymbol{x}) = d(\boldsymbol{x})\, \forall \boldsymbol{x} \in \Omega_c \tag{14}$$

which is introduced to couple the locality and non-locality of the decomposed strain fields such that the following continuity condition in the coupled strain field will be met under the Galerkin meshfree framework using the direct nodal integration scheme.

$$[[\bar{\boldsymbol{\varepsilon}}]]_{\Gamma_d} = \bar{\boldsymbol{\varepsilon}}^b(\boldsymbol{x}) - \bar{\boldsymbol{\varepsilon}}^c(\boldsymbol{x}) = 0 \quad for \quad \boldsymbol{x} \in \Gamma_d \tag{15}$$

In original strain-morphed nonlocal meshfree method [58], the stabilization strain field $\tilde{\boldsymbol{\varepsilon}}$ is introduced to the standard variational formulation through a penalty approach. It leads to a dual stress point integration scheme [57,58] for the evaluation of stress/strain fields. In other words, the evaluation of Eq. (9) involves two stress (strain) points at each meshfree node, one for nodal stress with regularization effect and the other for the stabilization. This dual stress point integration scheme will be discussed in Sect. 4 for the combined continuous–discontinuous approach.

3 The interactive particle enrichment algorithm for crack propagation

When the damage variable is close to one, the material is considered fully degraded, and the transition from damage to crack will be triggered in the combined continuous–discontinuous approach. Theoretically the precise location of crack initiation is a natural outcome of the damage evolution process and thus no initial crack needs to be defined in priori [11]. In practice, this crack usually initiates at the domain boundary. For most mesh-based numerical methods, this implies that crack should initiate at the integration point based on the Gaussian quadrature rule used for the domain integration. Therefore, an extrapolation scheme [11] is often needed to obtain the position of initial crack on the domain boundary for the associated element cutting in crack propagation simulation. In contrast to the existing discontinuous approaches in mesh-based numerical methods, an interactive particle enrichment algorithm is introduced to the strain-morphed nonlocal meshfree method [58] for the initiation and propagation of the crack, as described below.

First, an initial crack is defined on the original configuration by inserting an enriched particle at the midpoint of two regular particles in nearest neighbor as shown in Fig. 2, whenever their averaged damage value reaches 0.8. Subsequently, a simple averaging scheme is performed as an interpolation step using these two regular particles to obtain the averaged velocity, current position and internal variables for the enriched particle. This numerical interpolation step follows by a reconstruction of the meshfree approximation for the displacement field based on the insertion of enriched particle. Consequently, the strain-morphed nonlocal strain field is approximated and the computation proceeds. This initial crack will not propagate until the damage value of the

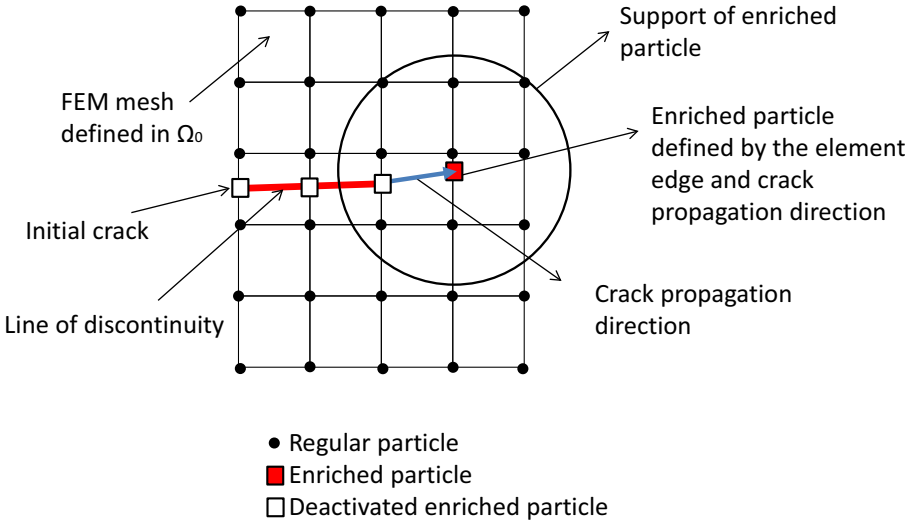

Fig. 2 The interactive particle enrichment of a cracked body defined in the un-deformed configuration

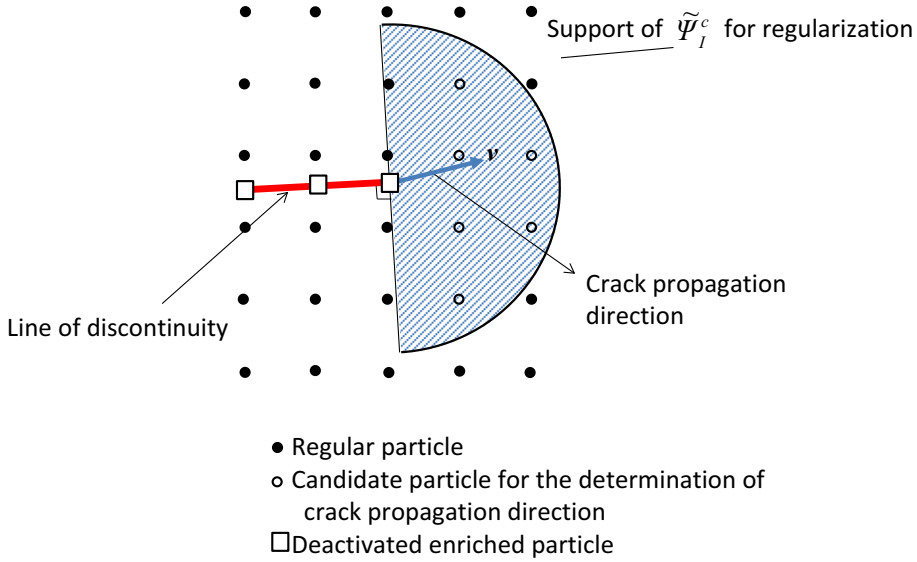

Fig. 3 The crack propagation direction is determined by damaged particles within the support of influence function for regularization

enriched particle is approaching to one (or numerically 0.95 in this study).

As soon as the initial crack starts to propagate, the extension of discontinuity needs to be made which requires the determination of crack propagation direction. Several approaches have been proposed for the determination of crack propagation direction in ductile fracture analysis [11,24]. In this paper we follow the approach of [24] and assume that no crack branching occurs in ductile fracture process. At first, a damage center $\boldsymbol{p}$ in front of the initial crack is determined in the reference configuration by

$$\boldsymbol{p} = \sum_{I \in G_K} \frac{\boldsymbol{X}_I \exp\left(d\left(\boldsymbol{X}_I\right)\right)}{\sum_{J \in G_K} \exp\left(d\left(\boldsymbol{X}_J\right)\right)} \tag{16}$$

where the G_k is a node set that collects all the candidates of particles within the first half of the domain of influence in strain smoothing function $\tilde{\Psi}^c(\mathbf{X})$ as shown in Fig. 3. In other words, the damage value is weighted with the exponential function in Eq. (16) for the determination of the damage center $\boldsymbol{p}$. With the defined damage center, the crack is assumed to advance in a direction given by

$$\boldsymbol{v} = \sum_{I \in G_K} \frac{\left(\boldsymbol{X}_I - \boldsymbol{p}\right) \exp\left(d\left(\boldsymbol{X}_I\right)\right)}{\sum_{J \in G_K} \exp\left(d\left(\boldsymbol{X}_J\right)\right)} \tag{17}$$

The main reason of obtaining the crack propagation direction in the reference configuration is same as that for most discontinuous approaches in fracture analysis [21,25]. That is to avoid the reformulation of the weak form problem due to the moving discontinuities. The second reason is to abstain from the tensile instability when the meshfree Lagrangian kernel is adopted to approximate the weak form solution, and this will be elaborated in the next section.

While the direction of discontinuity line is determined in the crack propagation step, the location of discontinuity front remains to be predicted. Numerically, the discontinuity front is defined to service as the location for next enriched particle. In this paper, the location of discontinuity front is determined by the intersection of the extension of discontinuity line and the edge of finite element ahead of the current enriched particle as shown in Fig. 2. Once the discontinuity front is determined and new particle is enriched, the old enriched particle is deactivated from the computation to respect the stress-free condition when the material is fully degraded. Under this scenario, the deactivated particle behaves like a crack tip that defines a transition point from continuous description to discontinuous description in the crack propagation step. Different from the crack tip in discrete approach that is aimed to approximate the near-singular stress fields for brittle fracture analysis, the crack tip in this combined continuous–discontinuous approach is in stress-free condition which is a natural outcome of the degrading constitutive response in the ductile materials. In other words, the need of an approximation for strain singularity at the crack tip can be inherently bypassed. As a result, the compatibility between the continuum damage mechanics and the bonded strain field continues to sustain. In essence, a finite size damage process zone is always formed ahead of the crack tip. It is worthwhile to remark that without the introduction of strain non-locality to the damage process zone, the damage growth rate will tend to become infinite at the crack tip, resulting in a prompt fracture as in the brittle material when the discretized model is continuously refined. This type of discretization sensitivity phenomenon in the combined continuous–discontinuous approach can be tackled down by the strain-morphed nonlocal strain method [58] and will be demonstrated in the numerical examples.

Subsequently, the interpolation step using the meshfree shape functions is taken to obtain the independent and dependent field variables for the newly enriched particle. By connecting the traction-free piecewise-continuous line of discontinuity as shown in Fig. 4, the visibility criteria [28] can be pursued to construct the new approximation for the displacement field as well as the strain-morphed nonlocal strain field in the cracked body. Same numerical procedure as that in the initial crack situation repeats for whole crack propagation steps till the end of simulation. A high-level overview of the interactive particle enrichment algorithm is provided in Fig. 5.

4 Variational formulation and discrete equations

To introduce the stabilization and regularization strain fields into the Galerkin method for the combined continuous–discontinuous approach, we follow closely the works in [53,58]. For simplicity, we assume the homogenous Dirichlet problem in the following variational derivation. The admissible space for the displacement fields is defined by

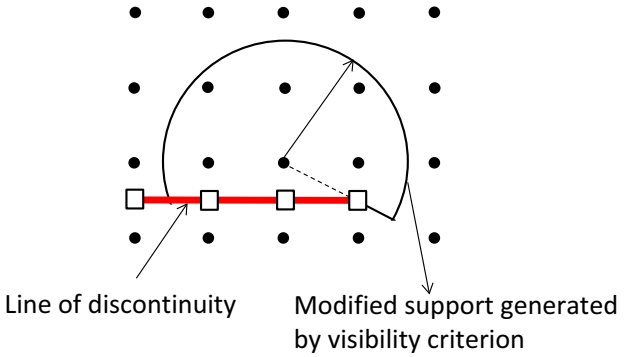

Fig. 4 The modified particle support produced by the visibility criterion

$$\boldsymbol{V}^h(\Omega) = \left\{ \boldsymbol{v} : \boldsymbol{v} \Big|_{\Omega} \in \boldsymbol{H}^1(\Omega), \boldsymbol{v} = \boldsymbol{0} \quad on \quad \partial\Omega \right\} \tag{18}$$

For a particle distribution denoted by an index set $Z_I = \{\boldsymbol{x}_I\}_{I=1}^{NP}$, we approximate the displacement field using the meshfree approximation to give

$$\boldsymbol{u}^h(\boldsymbol{x}) = \sum_{I=1}^{NP} \phi_I^a(\boldsymbol{x})\, \tilde{\boldsymbol{u}}_I \equiv \hat{\boldsymbol{u}}(\boldsymbol{x}) \; \forall \boldsymbol{x} \in \Omega \tag{19}$$

where NP is the total number of particles in discretization. $\phi_I^a(\boldsymbol{x})$, I=1,...NP can be considered as the shape functions of the meshfree approximation for displacement field $\boldsymbol{u}^h(\boldsymbol{x})$. Note that the radius size a of $\phi_I^a(\boldsymbol{x})$ is a numerical length parameter in meshfree displacement approximation. In this study $a = b$ (for stabilization) is used for all numerical investigations. In general, $\tilde{\boldsymbol{u}}_I$ is not the physical particle displacement and is often referred to as the "generalized displacement" [61] of particle I in Galerkin meshfree method. As a result, special essential boundary condition treatment is needed. To simplify the enforcement of essential boundary condition in this study, a first-order meshfree convex approximation [62] is considered. They are constructed by the Generalized Meshfree Approximation (GMF) method (see [62] for detail mathematical derivation and [63] for the nonlinear formulations in general solid mechanics applications). With the meshfree convex approximation, we can define the $\boldsymbol{H}_0^1$-conforming subspace for the approximation of displacement field to be

$$\boldsymbol{V}^h := \text{span}\left\{ \phi_I^a \Big| \left(supp\ \phi_I^a\right)^0 \subset \Omega, \quad I \in Z_I \right\} \tag{20}$$

Using the defined approximation space, the weak form for the given problem in Sect. 2 can be obtained based on the

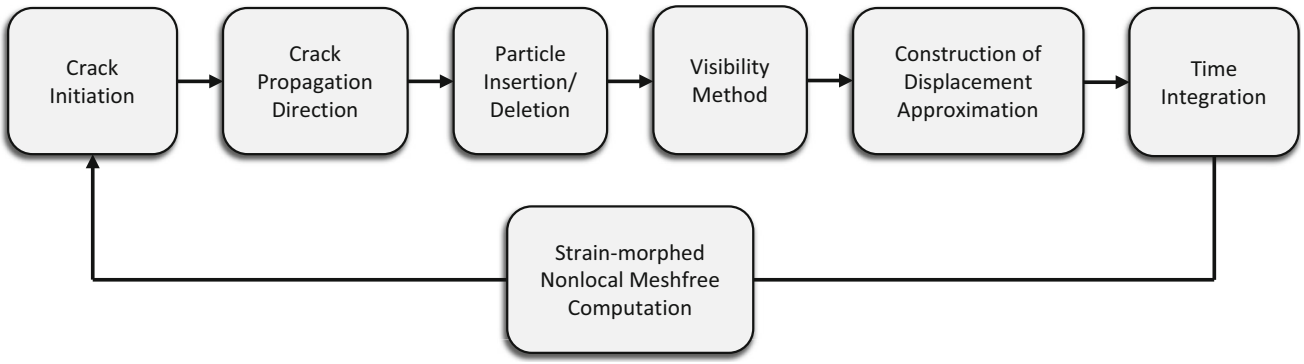

Fig. 5 The high-level overview of the interactive particle enrichment algorithm

penalized variational formulation [57] through an updated Lagrangian approach with reference to the current configuration in the elastic–plastic-damage analysis to find $\hat{\boldsymbol{u}}(\boldsymbol{x}) \in \boldsymbol{V}^h$

$$\begin{aligned}\int_{\Omega\backslash\Gamma_f} \delta\hat{\boldsymbol{u}}\cdot\rho\ddot{\hat{\boldsymbol{u}}}d\Omega &= \int_{\Omega_b} \delta\left(\boldsymbol{\varepsilon}\left(\hat{\boldsymbol{u}}\right)\right)^T : \boldsymbol{\sigma}d\Omega \\ &+ \int_{\Omega_c} \delta\left(\boldsymbol{\varepsilon}\left(\hat{\boldsymbol{u}}\right) + \pi\left(\boldsymbol{x}\right)\nabla^{(2)}\boldsymbol{\varepsilon}\left(\hat{\boldsymbol{u}}\right)\cdot^{(2)}\boldsymbol{\eta}^c\left(\boldsymbol{x}\right)\right)^T : \boldsymbol{\sigma}d\Omega \\ &+ \int_{\Omega\backslash\Gamma_f} \delta\left(\nabla\boldsymbol{\varepsilon}\left(\hat{\boldsymbol{u}}\right)\cdot\boldsymbol{\lambda}^b\left(\boldsymbol{x}\right)\right)^T : \tilde{\boldsymbol{\sigma}}d\Omega \\ &- \int_{\Gamma_d} \delta\left[\left[\hat{\boldsymbol{u}}\right]\right]\cdot\boldsymbol{t}^c d\Gamma - l^{ext}\left(\hat{\boldsymbol{u}}\right), \quad \forall\delta\hat{\boldsymbol{u}} \in \boldsymbol{V}^h \end{aligned} \tag{21}$$

$$l^{ext}\left(\hat{\boldsymbol{u}}\right) = \int_{\Omega\backslash\Gamma_f} \delta\hat{\boldsymbol{u}}\cdot\rho\boldsymbol{b}d\Omega + \int_{\Gamma_h} \delta\hat{\boldsymbol{u}}\cdot\boldsymbol{h}d\Gamma \tag{22}$$

where $\boldsymbol{\sigma}$ is the Cauchy stress obtained by direct nodal integration scheme. The update of Cauchy stress $\boldsymbol{\sigma}$ using the non-local elastic–plastic-damage model follows closely the existing literature [64,65] and is summarized in the Appendix. $\boldsymbol{\lambda}^b$ and $\boldsymbol{\eta}^c$ are coefficient matrices for stabilization and regularization shown in Eq. (11) and Eq. (13), respectively. The penalty term in Eq. (21) contains an enhanced stress field $\tilde{\boldsymbol{\sigma}}$ for stabilization. Note that stress quantities in Eq. (21) are defined in the current configuration Ω. The enhanced stress field used for stabilization in the nonlinear analysis is formulated using a material response tensor (elasto-plastic tangent modulus) $\boldsymbol{C}^\sigma$ and damage variable d as [58]

$$\tilde{\boldsymbol{\sigma}} = (1-d)\,\boldsymbol{C}^\sigma : \left(\nabla\boldsymbol{\varepsilon}\left(\hat{\boldsymbol{u}}\right)\cdot\boldsymbol{\lambda}^b\right) \tag{23}$$

For simplicity, it is assumed that no contact acts on the crack surfaces. Using the zero cohesive traction condition on the discontinuity line Γ_f from the interactive particle enrichment algorithm, Eq. (21) and (22) can be reduced to

$$\begin{aligned}\int_{\Omega\backslash\Gamma_f} \delta\hat{\boldsymbol{u}}\cdot\rho\ddot{\hat{\boldsymbol{u}}}d\Omega &= \int_{\Omega_b} \delta\left(\boldsymbol{\varepsilon}\left(\hat{\boldsymbol{u}}\right)\right)^T : \boldsymbol{\sigma}d\Omega \\ &+ \int_{\Omega_c} \delta\left(\boldsymbol{\varepsilon}\left(\hat{\boldsymbol{u}}\right) + \pi\left(\boldsymbol{x}\right)\nabla^{(2)}\boldsymbol{\varepsilon}\left(\hat{\boldsymbol{u}}\right)\cdot^{(2)}\boldsymbol{\eta}^c\left(\boldsymbol{x}\right)\right)^T : \boldsymbol{\sigma}d\Omega \\ &+ \int_{\Omega\backslash\Gamma_f} \delta\left(\nabla\boldsymbol{\varepsilon}\left(\hat{\boldsymbol{u}}\right)\cdot\boldsymbol{\lambda}^b\left(\boldsymbol{x}\right)\right)^T : \tilde{\boldsymbol{\sigma}}d\Omega - l^{ext}\left(\hat{\boldsymbol{u}}\right), \quad \forall\delta\hat{\boldsymbol{u}} \in \boldsymbol{V}^h \end{aligned} \tag{24}$$

$$l^{ext}\left(\hat{\boldsymbol{u}}\right) = \int_{\Omega\backslash\Gamma_f} \delta\hat{\boldsymbol{u}}\cdot\rho\boldsymbol{b}d\Omega + \int_{\Gamma_h} \delta\hat{\boldsymbol{u}}\cdot\boldsymbol{h}d\Gamma \tag{25}$$

Considering that the Lagrangian meshfree shape function [61,66], the gradients of displacement and strain approximations are defined in the reference configuration to avoid the tensile instability, the variation equations of Eqs. (24) and (25) are transformed from the current configuration Ω to the reference configuration Ω^0 as

$$\begin{aligned}\int_{\Omega^0\backslash\Gamma_f^0} \delta\hat{\boldsymbol{u}}\cdot\rho^0\ddot{\hat{\boldsymbol{u}}}d\Omega &= \int_{\Omega_b^0} \delta\left(\boldsymbol{F}^{-1}\boldsymbol{\varepsilon}\left(\hat{\boldsymbol{u}}\right)\right)^T : \boldsymbol{\sigma}J^0 d\Omega \\ &+ \int_{\Omega_c^0} \delta\left(\boldsymbol{F}^{-1}\left(\boldsymbol{\varepsilon}\left(\hat{\boldsymbol{u}}\right) + \pi\left(\boldsymbol{X}\right)\nabla^{(2)}\boldsymbol{\varepsilon}\left(\hat{\boldsymbol{u}}\right)\cdot\boldsymbol{\eta}^c\left(\boldsymbol{X}\right)\right)\right)^T : \boldsymbol{\sigma}J^0 d\Omega \\ &+ \int_{\Omega^0\backslash\Gamma_f^0} \delta\left(\boldsymbol{F}^{-1}\left(\nabla\boldsymbol{\varepsilon}\left(\hat{\boldsymbol{u}}\right)\cdot\boldsymbol{\lambda}^b\left(\boldsymbol{X}\right)\right)\right)^T : \tilde{\boldsymbol{\sigma}}J^0 d\Omega - l^{ext}\left(\hat{\boldsymbol{u}}\right) \end{aligned} \tag{26}$$

$$l^{ext}\left(\hat{\boldsymbol{u}}\right) = \int_{\Omega^0\backslash\Omega_f^0} \delta\hat{\boldsymbol{u}}\cdot\rho^0\boldsymbol{b}d\Omega + \int_{\Gamma_t^0} \delta\hat{\boldsymbol{u}}\cdot\boldsymbol{h}^0 d\Gamma \tag{27}$$

$$F_{ij}(\mathbf{X}) = \frac{\partial x_i(\mathbf{X})}{\partial X_j} = \sum_{I=1}^{NP} \frac{\partial\phi^\alpha(\mathbf{X})}{\partial X_j} x_{Ii} \tag{28}$$

where $\boldsymbol{F}$ is the deformation gradient, x_{Ii} denotes the i-component of current position at node I, and $\boldsymbol{X} = [X, Y]^T$ is a position vector defined in the reference configuration. J^0 is the determinant of the deformation gradient.

Using the first-order meshfree convex approximation [58,62] for $\phi^a(\boldsymbol{X})$ and zero-order strain smoothing function for $\tilde{\Psi}^b(\boldsymbol{X})$ and $\tilde{\Psi}^c(\boldsymbol{X})$ lead to the following discrete form of momentum equation to be solved by the combined

continuous–discontinuous approach for explicit dynamics analysis in damage-induced strain localization problem:

$$\boldsymbol{M}^{lump}\ddot{\boldsymbol{U}} = \boldsymbol{f}^{ext} - \boldsymbol{f}_b^{int} - \boldsymbol{f}_c^{int} - \tilde{\boldsymbol{f}}^{stab} \tag{29}$$

$$\boldsymbol{M}_I^{lump} = \sum_{N=1}^{NP} \rho^0 \phi_I^a(\boldsymbol{X}_N) V_N^0 \boldsymbol{I}_{[2\times 2]} \tag{30}$$

where $\boldsymbol{f}^{ext}$ is standard external force matrix, $\ddot{\boldsymbol{U}}$ is the matrix contains nodal accelerations. $\boldsymbol{V}_K^0$ is the initial nodal volume of node K, and $\boldsymbol{M}_I^{lump}$ is the lumped nodal mass matrix. Two internal force matrices are computed by the direct nodal integration scheme as

$$\boldsymbol{f}_{bI}^{\text{int}} = \int_{\Omega_b^0} \boldsymbol{B}_I^T \boldsymbol{\sigma} J^0 d\Omega \overset{DNI}{=} \sum_{N=1}^{NP} \boldsymbol{B}_I^T(\boldsymbol{X}_N) \boldsymbol{\sigma}(\boldsymbol{X}_N) J^0 V_N^0 \tag{31}$$

$$\boldsymbol{B}_I(\boldsymbol{X}) = \begin{bmatrix} b_{I1}(\boldsymbol{X}) & 0 \\ b_{I2}(\boldsymbol{X}) & b_{I1}(\boldsymbol{X}) \\ 0 & b_{I2}(\boldsymbol{X}) \end{bmatrix} \tag{32}$$

$$b_{I1}(\boldsymbol{X}) = \phi_{I,x}^a(\boldsymbol{X}) \quad \text{and} \quad b_{I2}(\boldsymbol{X}) = \phi_{I,y}^a(\boldsymbol{X}) \tag{33}$$

$$\begin{aligned} \boldsymbol{f}_{cI}^{\text{int}} = & \int_{\Omega_c^0} \left(\boldsymbol{B}_I + d(\boldsymbol{X}) \tilde{\tilde{\boldsymbol{B}}}_I\right)^T \\ & \times \sigma J^0 d\Omega \overset{DNI}{=} \sum_{N=1}^{NP} \left(\boldsymbol{B}_I(\boldsymbol{X}_N) + d(\boldsymbol{X}_N) \tilde{\tilde{\boldsymbol{B}}}_I\right)^T \\ & \times \boldsymbol{\sigma}(\boldsymbol{X}_N) J^0 V_N^0 \end{aligned} \tag{34}$$

$$\tilde{\tilde{\boldsymbol{B}}}_I(\boldsymbol{X}) = \begin{bmatrix} \tilde{\tilde{b}}_{I1}(\boldsymbol{X}) & 0 \\ \tilde{\tilde{b}}_{I2}(\boldsymbol{X}) & \tilde{\tilde{b}}_{I1}(\boldsymbol{X}) \\ 0 & \tilde{\tilde{b}}_{I2}(\boldsymbol{X}) \end{bmatrix} \tag{35}$$

$$\begin{aligned} \tilde{\tilde{b}}_{I1}(\boldsymbol{X}) = & \alpha_{\text{xx}}(\boldsymbol{X}) \phi_{I,\text{xxx}}^a(\boldsymbol{X}) + 2\alpha_{\text{xy}} \phi_{I,\text{xxy}}^a(\boldsymbol{X}) \\ & + \alpha_{\text{yy}}(\boldsymbol{X}) \phi_{I,\text{xyy}}^a(\boldsymbol{X}) \end{aligned} \tag{36}$$

$$\begin{aligned} \tilde{\tilde{b}}_{I2}(\boldsymbol{X}) = & \alpha_{\text{xx}}(\boldsymbol{X}) \phi_{I,\text{yxx}}^a(\boldsymbol{X}) + 2\alpha_{\text{xy}} \phi_{I,\text{yxy}}^a(\boldsymbol{X}) \\ & + \alpha_{\text{yy}}(\boldsymbol{X}) \phi_{I,\text{yyy}}^a(\boldsymbol{X}) \end{aligned} \tag{37}$$

$$\alpha_{\text{xx}}(\boldsymbol{X}) = \frac{1}{2} \sum_{J=1}^{NP} \tilde{\Psi}_J^c(\boldsymbol{X}) (X_J - X)^2 \tag{38}$$

$$\alpha_{\text{xy}}(\boldsymbol{X}) = \frac{1}{2} \sum_{J=1}^{NP} \tilde{\Psi}_J^c(\boldsymbol{X}) (X_J - X)(Y_J - Y) \tag{39}$$

$$\alpha_{\text{yy}}(\boldsymbol{X}) = \frac{1}{2} \sum_{J=1}^{NP} \tilde{\Psi}_J^c(\boldsymbol{X}) (Y_J - Y)^2 \tag{40}$$

Finally, the stabilized force matrix is also computed by the direct nodal integration scheme as

$$\tilde{\boldsymbol{f}}_I^{stab} = \int_{\Omega^0} \tilde{\boldsymbol{B}}_I^T \tilde{\boldsymbol{\sigma}} J^0 d\Omega \overset{DNI}{=} \sum_{N=1}^{NP} \tilde{\boldsymbol{B}}_I^T(\boldsymbol{X}_N) \tilde{\boldsymbol{\sigma}}(\boldsymbol{X}_N) J^0 V_N^0 \tag{41}$$

The first-order strain-gradient matrix $\tilde{\boldsymbol{B}}_I$ in Eq. (41) is given by

$$\tilde{\boldsymbol{B}}_I(\boldsymbol{X}) = \begin{bmatrix} \tilde{b}_{I1}(\boldsymbol{X}) & 0 \\ \tilde{b}_{I2}(\boldsymbol{X}) & \tilde{b}_{I1}(\boldsymbol{X}) \\ 0 & \tilde{b}_{I2}(\boldsymbol{X}) \end{bmatrix} \tag{42}$$

The components of the first-order strain-gradient matrix $\tilde{B}_I$ are

$$\tilde{b}_{I1}(\boldsymbol{X}) = \beta_{\text{x}}(\boldsymbol{X}) \phi_{I,\text{xx}}^a(\boldsymbol{X}) + \beta_{\text{y}}(\boldsymbol{X}) \phi_{I,\text{xy}}^a(\boldsymbol{X}) \tag{43}$$

$$\tilde{b}_{I2}(\boldsymbol{X}) = \beta_{\text{x}}(\boldsymbol{X}) \phi_{I,\text{yx}}^a(\boldsymbol{X}) + \beta_{\text{y}}(\boldsymbol{X}) \phi_{I,\text{yy}}^a(\boldsymbol{X}) \tag{44}$$

$$\beta_{\text{x}}(\boldsymbol{X}) = \sum_{J=1}^{NP} \tilde{\Psi}_J^b(\boldsymbol{X}) (X_J - X) \tag{45}$$

$$\beta_{\text{y}}(\boldsymbol{X}) = \sum_{J=1}^{NP} \tilde{\Psi}_I^b(\boldsymbol{X}) (Y_J - Y) \tag{46}$$

$\tilde{\boldsymbol{\sigma}}^T = (\tilde{\sigma}_{11}, \tilde{\sigma}_{12}, \tilde{\sigma}_{22})$ is a vector containing the component of Cauchy stress associated with the stabilization. Since the numerical evaluation of stabilized stress vector using Eq. (23) is computationally unfeasible [57] in explicit dynamics analysis, the nodal stabilized stress vector is updated using the incremental stabilized stress vector suggested by Belytschko and Lee [67] as follows

$$\tilde{\boldsymbol{\sigma}}_{n+1} = \tilde{\boldsymbol{\sigma}}_n + \Delta\tilde{\boldsymbol{\sigma}}_{n+1} = \tilde{\boldsymbol{\sigma}}_n + 2\tilde{G}(1-d)\left(\tilde{\boldsymbol{B}}_{dev}\right) \Delta\boldsymbol{u}_{n+1} \tag{47}$$

where $\tilde{G}$ is called the "modified shear modulus" [67] which is computed by

$$2\tilde{G} = \sqrt{\frac{H_{\Delta\tau}}{H_{\Delta e}}} \tag{48}$$

$$H_{\Delta\tau} = \frac{1}{2} \sum_{i=1}^{2} \sum_{j=1}^{2} \Delta\tau_{ij} \Delta\tau_{ij}, \quad H_{\Delta e} = \frac{1}{2} \sum_{i=1}^{2} \sum_{i=1}^{2} \Delta e_{ij} \Delta e_{ij} \tag{49}$$

$\Delta\tau_{ij}$ and Δe_{ij} are the components of deviatoric part of the stress and strain increments, respectively. they are obtained from the regularized nodal stress and strain computation. $\tilde{\boldsymbol{B}}_{dev}$ is the deviatoric part of first-order strain-gradient matrix $\tilde{\boldsymbol{B}}$.

The computation of Eq. (29) involves two coinciding stress points at each meshfree node, one for nodal stress

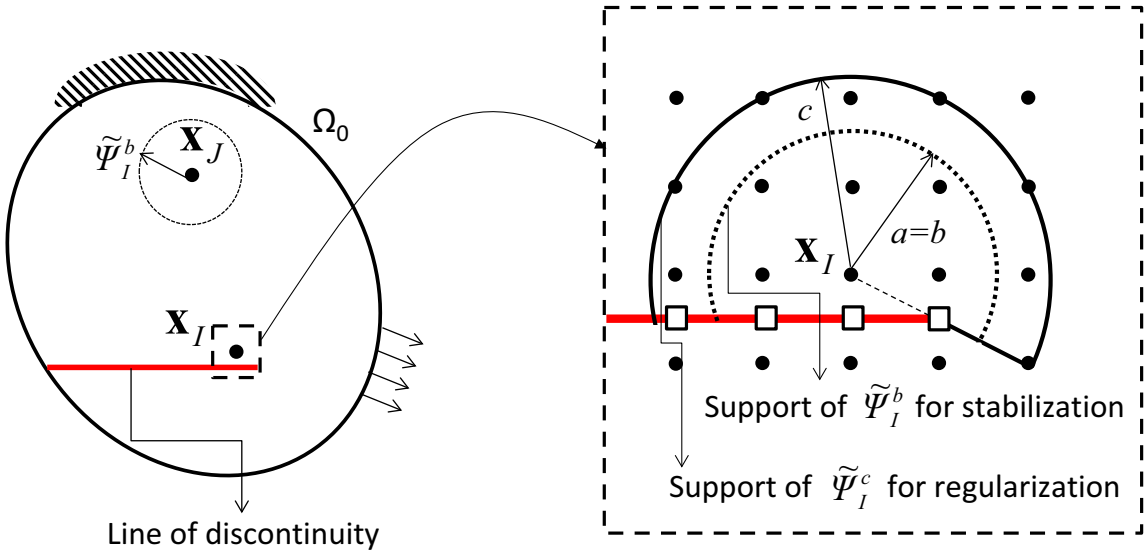

Fig. 6 Illustration of dual stress points and the modified supports of two influence functions in present method

$\boldsymbol{\sigma}$ with regularization effect and the other for the enhanced nodal stress $\tilde{\boldsymbol{\sigma}}$ for the necessary stabilization. This dual stress point integration scheme is illustrated in a cracked body as shown in Fig. 6 using the interactive particle enrichment algorithm. Finally, the critical time step for the central difference time integration in the explicit dynamics analysis is governed by the Courant–Friedrichs–Lewy (CFL) condition and is determined from the development in [57] for the numerical study. It is worthwhile to note that the meshfree time steps in the explicit dynamics analysis are controlled implicitly [68] by the radius size a of $\phi_I^a(\boldsymbol{x})$ in the displacement approximation instead of the closet nodal distance or element size in finite element method; therefore they will not be cut down abruptly due to an insertion of the discontinuity.

5 Numerical examples

In this section, three benchmark examples are analyzed to study the performance of present method in the ductile fracture analysis. Plain stress condition is assumed in two-dimensional problems. Unless otherwise specified, a normalized nodal support size of 2.0 is used for the radius size of meshfree shape functions ϕ^a and strain smoothing function $\tilde{\Psi}^b$ for stabilization. In all test cases, we have used the first-order meshfree convex approximations [62] for meshfree shape functions ϕ^a in the displacement approximation to simplify the enforcement of boundary conditions. The Shepard function [62] is considered for the strain smoothing function $\tilde{\Psi}^b$ and $\tilde{\Psi}^c$ in this study.

A simple damage law is taken [34,58] in the following form for the demonstration purpose.

$$d = g(\kappa) \tag{50}$$

$$g(\kappa) = \begin{cases} \frac{\kappa_c(\kappa-\kappa_i)}{\kappa(\kappa_c-\kappa_i)} & if \quad \kappa_i \le \kappa \le \kappa_c \\ 0.99 & if \quad \kappa > \kappa_c \end{cases} \tag{51}$$

where κ_i and κ_c denote the initial and critical values of effective plastic strain κ , respectively. In other words, it is assumed that failure occurs mainly due to plastic straining. The development of a physical-based damage law for the combined continuous–discontinuous approach may include the effect of the hydrostatic stress which is material dependent and is not within the scope of the paper. However it will be considered in the future study together with the experimental validation.

5.1 A tension mode test

In this example, a plate with two notches in a mode-I ductile fracture is analyzed as shown in Fig. 7. The notched plate is fixed on the bottom and is pulled in tension on the other end under the displacement control at speed of 1.0 mm/sec. Only half of the model is considered in simulation due to the symmetry of the geometry and boundary conditions. The material

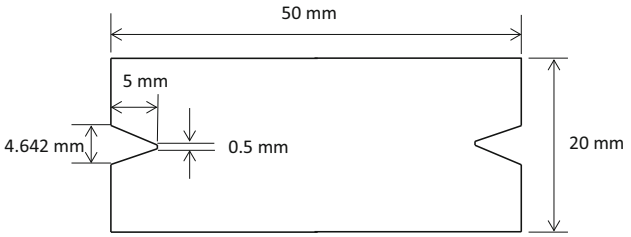

Fig. 7 The notched plate for tension mode ductile fracture simulation

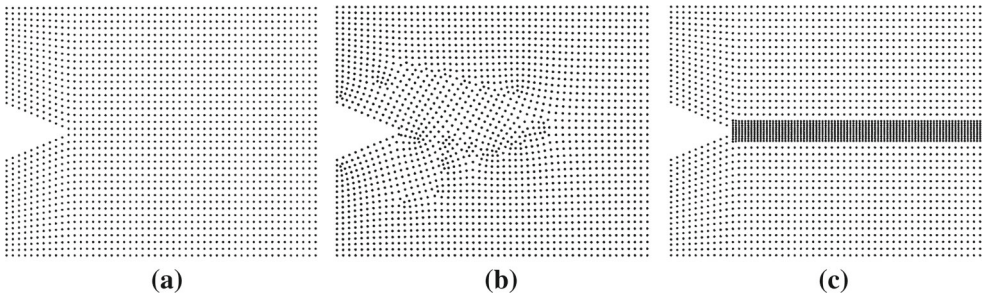

Fig. 8 Three types of discretization in the notched problem. **a** Coarse model (1938 nodes). **b** non-uniform model (2015 nodes), **c** locally refined model (2821 nodes)

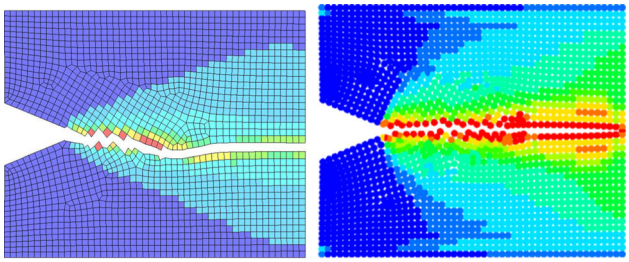

Fig. 9 The sensitivity study on mesh orientation using non-uniform discretization model. **a** Standard FEM with element erosion. **b** The present method

has an initial density $\rho^0 = 7800\,\text{kg/m}^3$. The strain-hardening elastic-plastic material properties are: Young's modulus $E = 180206.0$ MPa, Poisson's ratio $v = 0.3$, and an isotropic hardening rule $\sigma_y(\bar{e}^p) = \sigma_y^0(1+\alpha\bar{e}^p)^\beta$ with coefficients $\beta = 0.0513825$, $\sigma_y^0 = 1400.0$ MPa, and $\alpha = 2.5\text{e}4$. $\sigma_y(\bar{e}^p)$ is the flow stress which is a scalar and increases monotonically with the effective plastic strain $\bar{e}^p$. The damage parameters in Eq. (51) are: $\kappa_i = 0.05$, and $\kappa_c = 0.1$. Three types of discretization consisting of the coarse, non-uniform and locally refined models as displayed in Fig. 8a–c, respectively, are considered for the analysis. In the present continuous–discontinuous approach, the radius size c of $\tilde{\Psi}^c(X)$ for regularization is taken to be 1.0 mm for all discretization models.

To illustrate the mesh orientation sensitivity problem in the standard finite element method, a simulation using non-uniform discretization in Fig. 8b with bi-linear elements and element erosion technique is conducted. The crack propagation result displayed in Fig. 9a shows a strong dependence of mesh orientation on the crack propagation path using the standard finite element method. In contrast to the finite element solution, a discretization-objective solution of the proposed continuous–discontinuous approach is presented in Fig. 9b using same non-uniform discretization model.

The importance of strain regularization in the ductile fracture analysis is demonstrated in the next numerical study. Same problem is analyzed using the present continuous–discontinuous approach without an incorporation of regularization in strains. This can be done by simply setting the morphing function $\pi(\boldsymbol{x})$ to become zero in Eq. (26). Figure 10 displays the propagation of crack at t = 0.15 s in different discretization. Although the crack propagation path is not sensitive to the randomness and density of nodal distribution, the results in Fig. 10 do indicate that crack propagation speed is sensitive to the discretization. The plot of crack tip position vs time is given in Fig. 11a which confirms the discretization sensitivity results on the crack propagation speed. As a result, the response of reaction force varies dramatically in different discretization as shown in Fig. 12a. The discretization-dependent results of crack propagation speed and reaction force can be minimized with the introduction of strain regularization in the present continuous–discontinuous approach. As shown in Fig. 13, the tension mode of ductile fracture is well-captured with similar crack propagation speed in different discretization models. The discretization-independent result using the present continuous–discontinuous approach is also presented in Figs. 11b and 12b for the growth of crack and the reaction force response, respectively.

5.2 Double-notched specimen in simple tension test

A tensile test on another double-notched specimen is studied in this example. The geometry and boundary condition of the problem are given in Fig. 14, where the two ends of the specimen is subjected to a displacement control at speed of 0.5 mm/sec. Same material constants from example 1 are considered for the numerical analysis. Three levels of discretization as shown in Fig. 15 are utilized to study the convergence of the present method. The radius size c of $\tilde{\Psi}^c(\boldsymbol{X})$ for regularization in the present method is taken to be 1.60 mm for all discretization models.

The problem is first analyzed using the present continuous–discontinuous approach without the incorporation of the regularization in strains. As expected, the sensitive results in crack length are observed in the convergence study as shown

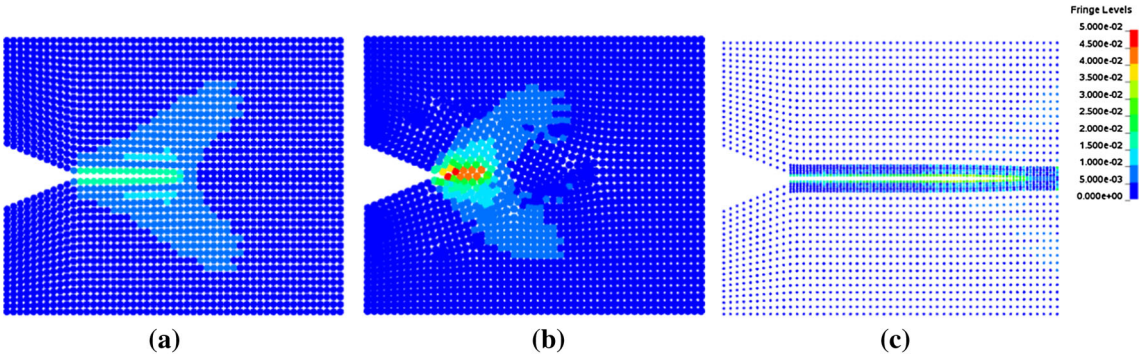

Fig. 10 The discretization sensitivity results of crack length and effective plastic strain contour at t = 0.15 s in three types of discretization model using the local strain approximation. **a** Uniform model. **b** Non-uniform model. **c** Locally refined model

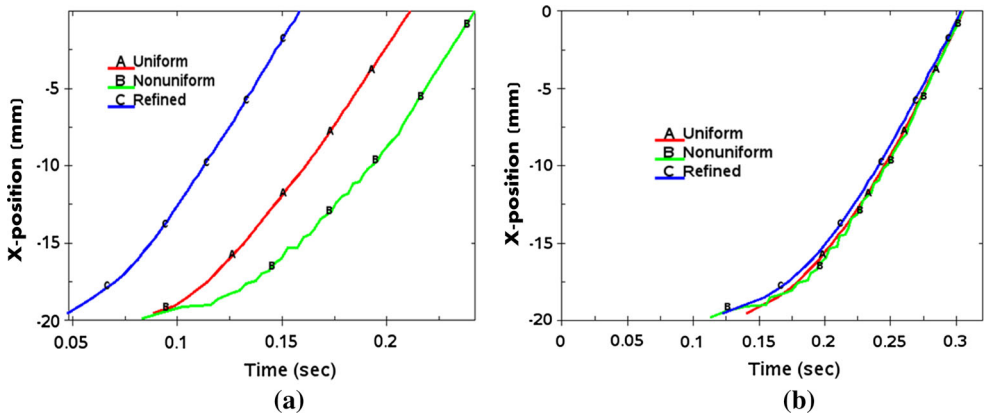

Fig. 11 Crack tip position-time history in the notched problem. **a** Local strain approximation. **b** Non-local approximation

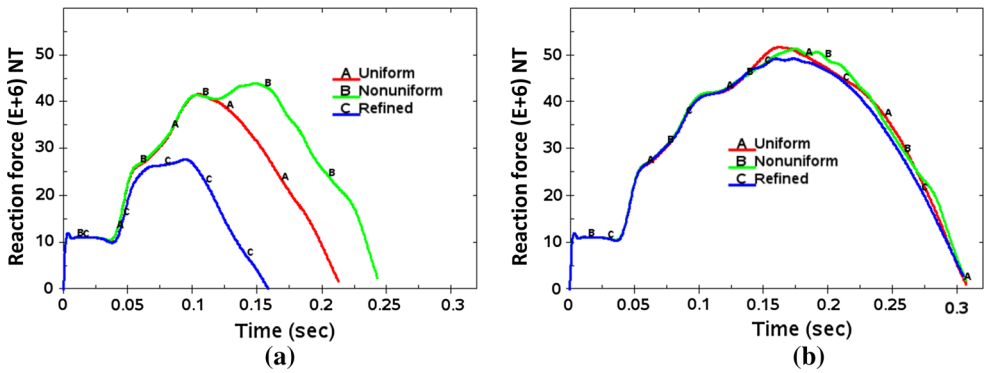

Fig. 12 Reaction force response in the notched problem. **a** Local strain approximation. **b** Non-local approximation

in Fig. 16 at t = 0.18 s. Figure 17a gives the reaction force response which indicates a strong pathological localization using the local strain approximation. In contrast, the present approach using the nonlocal strain approximation is able to regularize the pathologically localized solution as shown in Fig. 17b. The comparison of crack path displayed in the reference configuration is shown in Fig. 18. The convergence of final crack paths in three discretization models is given in Fig. 19, and a good correlation between two fine models is achieved. The effective plastic strain contours are plotted in the final deformed configuration as shown in Fig. 20a–c for three discretization models. The results in Fig. 20 suggest a comparable effective plastic strain distribution is obtained in three discretization models using the present combined continuous–discontinuous approach.

5.3 Double-notched specimen in bi-tension test

The ductile fracture under bi-tension effect is analyzed in this example. Same numerical model in example 5.2 with differ-

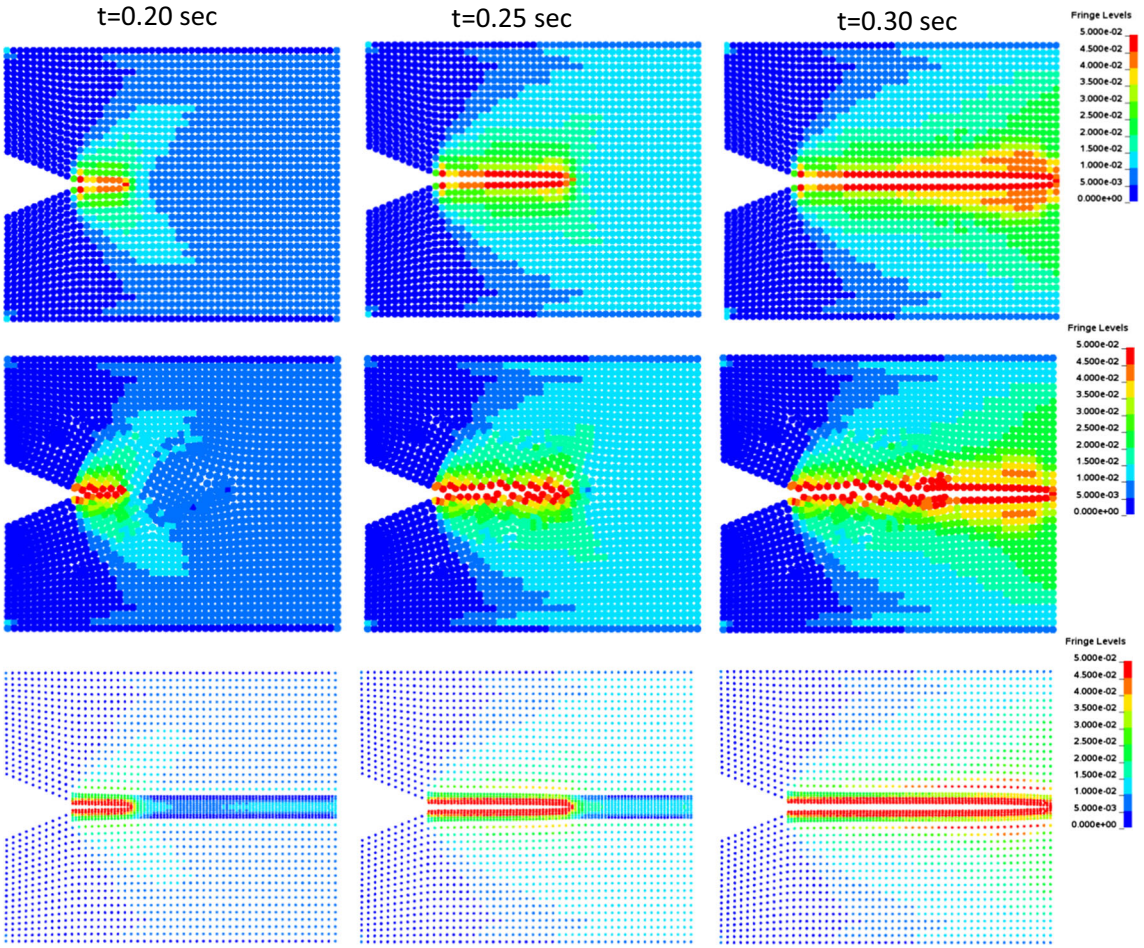

Fig. 13 The convergent results of crack propagation and effective plastic strain contour in three types of discretization model using the present strain-morphed nonlocal approximation

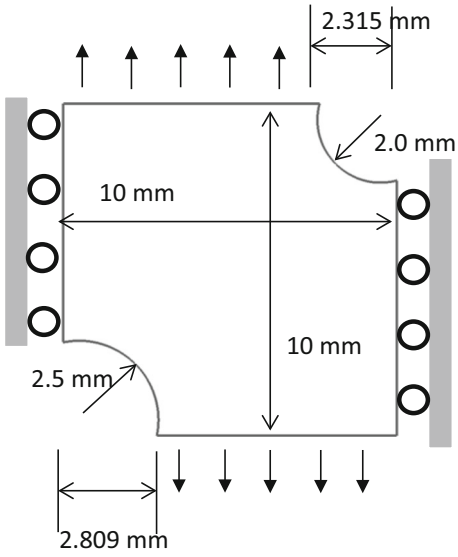

Fig. 14 The double-notched plate problem in simple tension test

ent boundary conditions is considered and given in Fig. 21. To study the difference of crack paths in bi-tension and simple tests, two material imperfections are initiated at same crack initiation position of example 5.2. The initial imperfection is defined to have a 30 % reduction of strength in the Young's modulus as that in the weak-discontinuity approach [58]. The specimen is subjected to a bi-axial displacement control at speed of 0.5 mm/s. Analogously three levels of discretization shown in Fig. 15 are utilized to study the convergence of the present method in bi-tension test.

Without the incorporation of strain regularization, the crack paths show strong discretization sensitivity as displayed in Fig. 22a–c for the coarse, fine and most fined models, respectively. The corresponding time-reaction force curves are plotted in Fig. 23a reflecting the non-convergent problem in the strain localization model. Superior performance of the present method is demonstrated in the convergence result of the crack paths in Fig. 24 and reaction force responses in Fig. 23b. Figure 25 compares the final

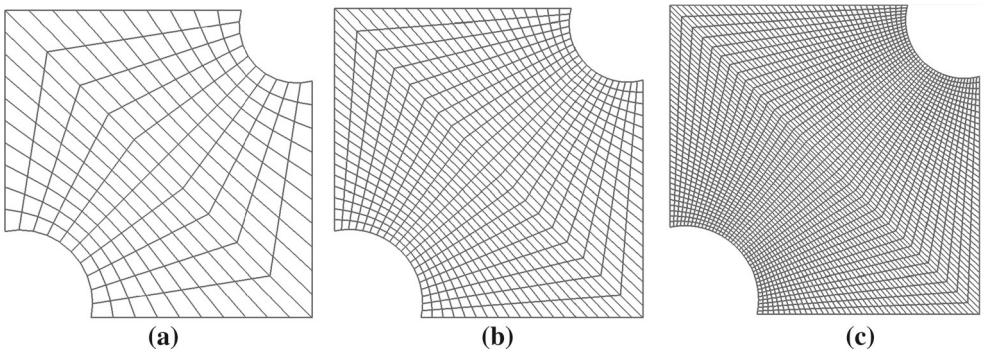

Fig. 15 Three types of discretization displayed in finite element mesh are adopted for the double-notched problem. **a** Coarse model (231 nodes). **b** Refined model (861 nodes). **c** Most refined model (3321 nodes)

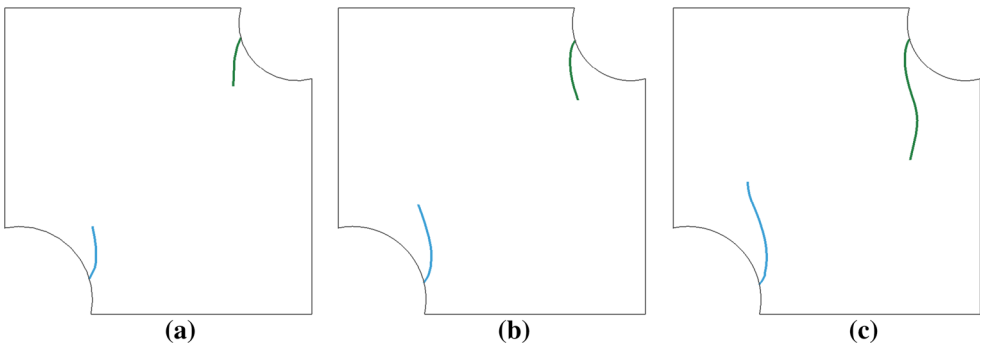

Fig. 16 The discretization sensitivity results of crack length at t = 0.18 s in three types of discretization model using the local strain approximation. **a** Coarse model. **b** Fine model. **c** Most refined model

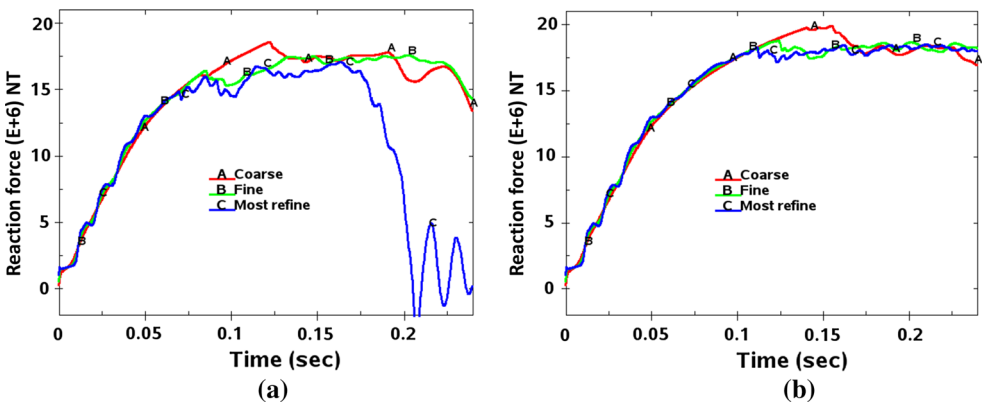

Fig. 17 Reaction force response in the notched problem. **a** Local strain approximation. **b** Non-local approximation

crack paths in three discretization models using the present continuous–discontinuous approach. Similar to the convergent result in the simple tension test, the crack path result in the bi-tension test does not exhibit strong discretization sensitivity. The final crack paths are plotted together with effective plastic strain contour as shown in Fig. 26a–c for the coarse, fine and most fined models, respectively. The patterns of crack path and effective plastic strain contour in two refined models are in good agreements.

6 Conclusions

In the combined continuous–discontinuous approach, ductile damage and fracture are considered within the same physical processes. Under this argument the continuous damage mechanics is utilized to macroscopically describe the degradation of ductile materials subjected to the evolution of micro-voids and micro-cracks in the average sense, while the displacement discontinuity is employed to provide a means

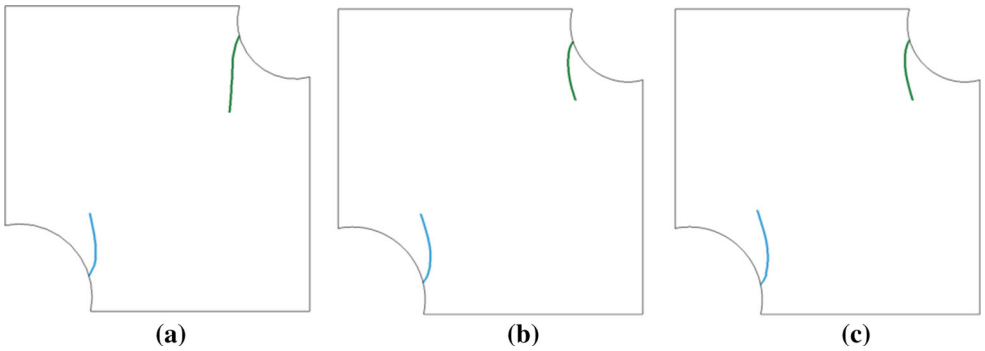

Fig. 18 The crack path at t = 0.24 s in three types of discretization model using the present strain-morphed nonlocal approximation. **a** Coarse model. **b** Fine model. **c** Most refined model

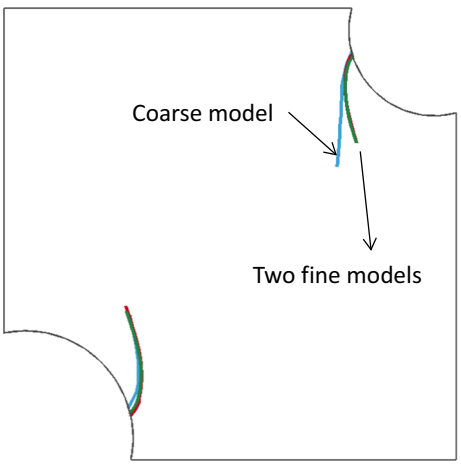

Fig. 19 The convergence of final crack paths in three discretization models using the present method

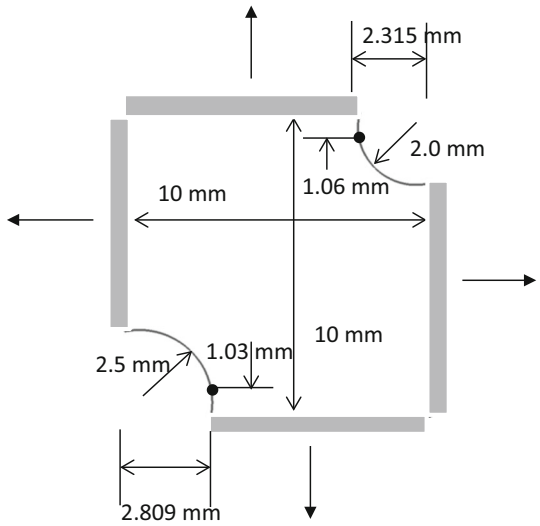

Fig. 21 The double-notched plate problem in bi-tension test

to mimic the macro-cracks in the final stage of continuous material failure when the damage field becomes critical. In this study the meshfree continuous–discontinuous approach is introduced to analyze this physical process. The present method combines the strain-morphed nonlocal meshfree method and the interactive particle enrichment algorithm to model the entire ductile fracture process from damage growth to crack propagation. Numerically, the present

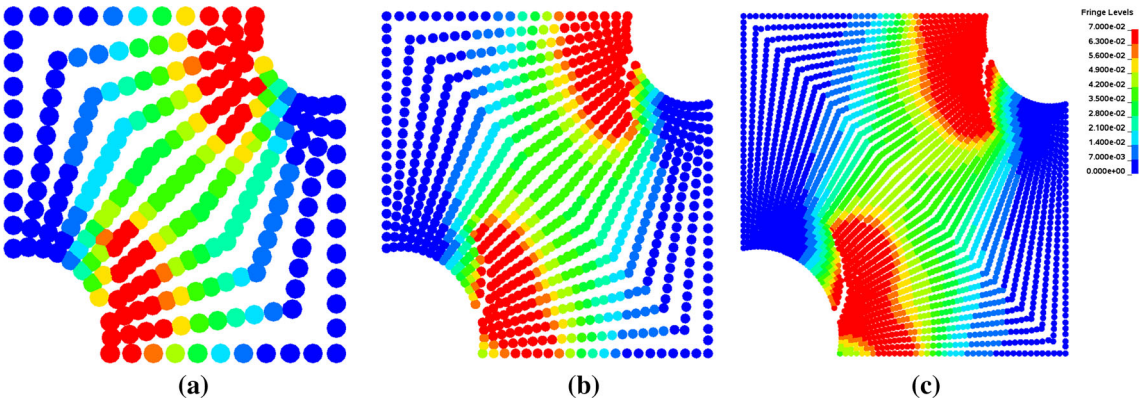

Fig. 20 The final crack path and effective plastic strain contour in three discretization models using the present method. **a** Coarse model. **b** Fine model. **c** Most refined model

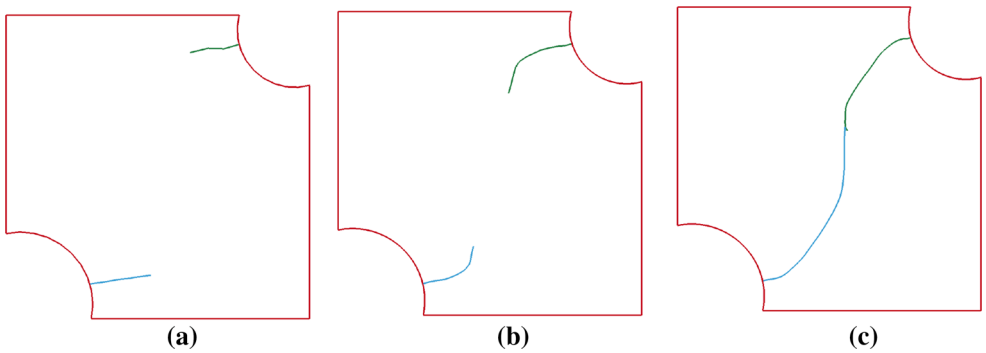

Fig. 22 The discretization sensitivity results of crack length at t = 0.17 s in three types of discretization model using the local strain approximation. **a** Coarse model. **b** Fine model. **c** Most refined model

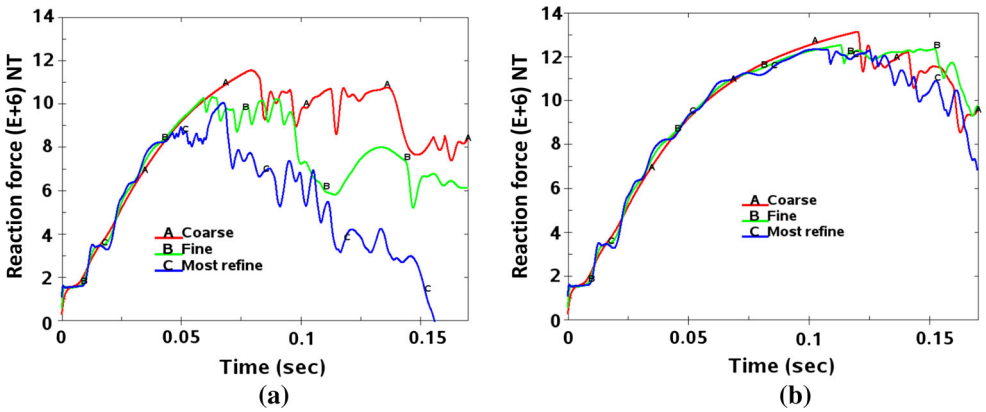

Fig. 23 Reaction force response in the bi-tension notched problem. **a** local strain approximation. **b** non-local approximation

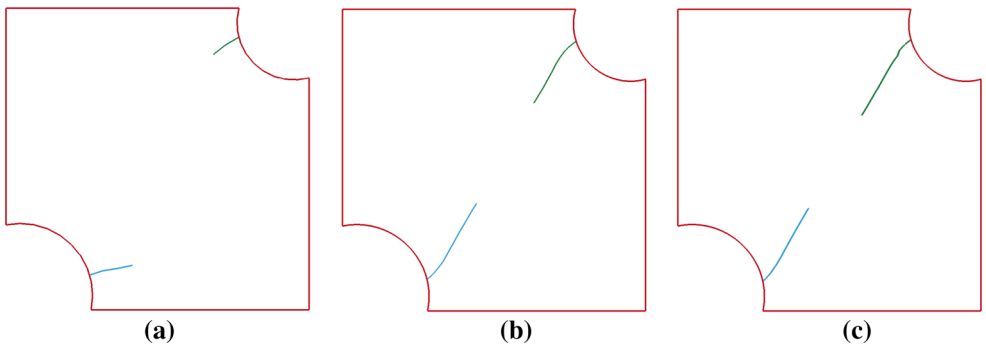

Fig. 24 The crack path at t = 0.17 s in three types of discretization model using the present strain-morphed nonlocal approximation. **a** Coarse model. **b** Fine model. **c** Most refined model

method improves the intrinsic implementation difficulties in existing meshfree regularization methods based on the background cells for domain integration. In comparison to the standard meshfree and finite element methods, the present method avoids some of the stability problems such as the spurious energy mode, pathological localization in the deformation and unrealistic damage growth. Since the present meshfree method is a pure nodal integration method, the abrupt drop of the explicit dynamic time steps due to the abnormal cut of elements in the mesh-based discontinuity enrichment approach can be effectively suppressed.

Three numerical benchmarks are studied to examine the effectiveness of the present approach. The numerical results in this study suggest that the present approach is able to

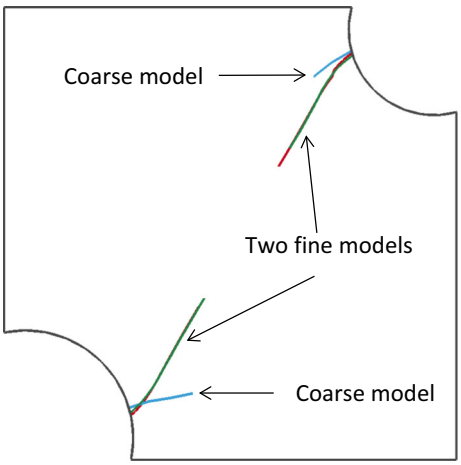

Fig. 25 The convergence of final crack paths in three discretization models using the present method

deliver stable, discretization-objective and convergent crack propagating solutions in the analysis of ductile fracture process. In particular, the patterns of the cracks in different discretization models are in good agreements throughout the simulation.

It is worthwhile to mention the regularization size of the present method in ductile fracture analysis for metals is considered a numerical parameter rather than a physical-based parameter, although many researchers [33,65] claim that the size of this parameter is related to the size of fracture process zone or maximum aggregate size in some materials such as concrete. From the phenomenological and computational view point, this numerical parameter is introduced in mathematical formulation such that the numerical solution tends to converge to a physically meaningful solution upon model refinement [65]. In other words, the nonlocal damage approach is motivated by experimental results with its numerical parameter calibrated from numerical simulations.

The incorporation of physical-based damage laws and different crack propagation criterion is material dependent and requires the experimental validation. Further results will be discussed in the near future. The applications of the present method to severe deformation problems and shell structures are under investigation. The extension of the present method to the three-dimensional explicit dynamics analysis will also be considered in the future.

Finally, the incorporation of the physical-based length scale for regularization in macroscopic analysis demands a multiscale or multiresolution computation since ductile fracture in metals depends strongly on the extreme values of microstructural characteristics. Recent multiscale and multiresolution approaches utilizing "simulation driven by experiments" technique [3,4] seem to be attractive for the analysis of non-uniform microstructures in heterogeneous alloys. Such approach becomes beneficial to the industrial applications if it can be cast within an efficient multiscale computational scheme.

Acknowledgments The authors would like to thank Dr. John O. Hallquist of LSTC for his support to this research. The financial support from Honda R&D Co., Ltd to LSTC and JSOL is greatly acknowledged.

Appendix

The combinations of isotropic damage and plasticity are widely used for ductile as well as semi-brittle fracture analyses. In this study, we follow a common approach [69–71] that combines the plasticity formulated on the effective stress $\bar{\boldsymbol{\sigma}}$ [5,6,9,33] with the strain-based damage.

For isotropic damage, the effective stress tensor $\bar{\boldsymbol{\sigma}}$ is related to Cauchy stress tensor $\boldsymbol{\sigma}$ by [5,6,9,33]

$$\bar{\boldsymbol{\sigma}} = \frac{\boldsymbol{\sigma}}{(1-d)} = \boldsymbol{C}^e : \boldsymbol{\varepsilon}^e = \boldsymbol{C}^e : \left(\boldsymbol{\varepsilon} - \boldsymbol{\varepsilon}^p\right) \tag{52}$$

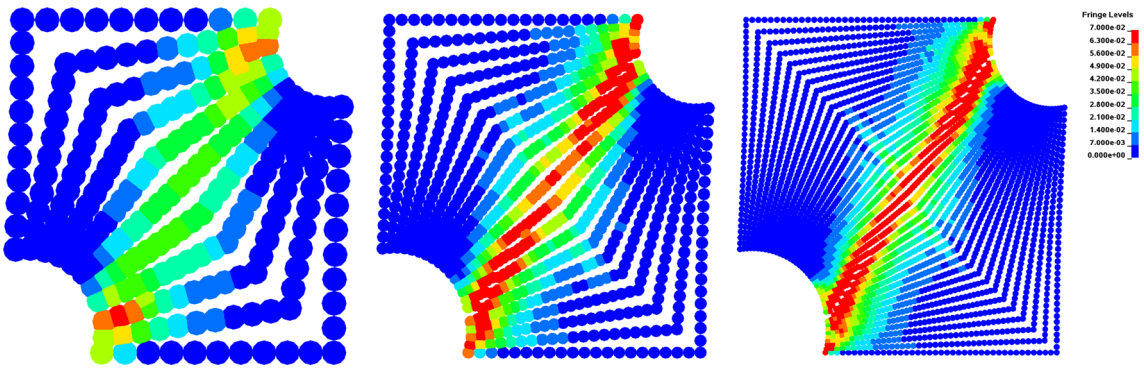

Fig. 26 The final crack path and effective plastic strain contour in three discretization models using the present method. **a** Coarse model. **b** Fine model. **c** Most refined model

where $\boldsymbol{C}^e$ is the fourth order elastic stiffness tensor, $\boldsymbol{\varepsilon}^e$ is the elastic strain, $\boldsymbol{\varepsilon}$ is the total strain, $\boldsymbol{\varepsilon}^p$ is the plastic strain and d is the scale damage valuable. Note in engineering practice, the evolution equations for international valuable d and $\boldsymbol{\varepsilon}^p$ are phenomenological and material dependent. The algorithm for the stress update in Eq. (52) is divided into two stages [64,65,71]. First, the update of effective stress for the plastic part is carried out by an implicit algorithm; then, the damage part is evaluated from the plastic strain increment obtained in the first stage.

In the first stage, the yield function is also defined in the effective stress space as [64,65]

$$\bar{\phi}^p\left(\bar{\boldsymbol{\tau}}, e^p\right) = \|\bar{\boldsymbol{\tau}}\| - \sqrt{\frac{2}{3}}\boldsymbol{\sigma}_y\left(e^p\right) \tag{53}$$

where $\bar{\tau}$ is the effective or undamaged deviatoric stress tensor, and σ_y is the flow stress. The local effective plastic strain e^p is defined as usual by

$$e^p = \int_0^t \sqrt{\frac{2}{3}}\left\|\dot{\boldsymbol{\varepsilon}}^p(s)\right\| ds \tag{54}$$

with the classical flow rule of associative plasticity given by

$$\dot{\boldsymbol{\varepsilon}}^p = \dot{\gamma}\frac{\partial\bar{\phi}^p}{\partial\bar{\boldsymbol{\sigma}}} = \dot{\gamma}\frac{\bar{\boldsymbol{\tau}}}{\|\bar{\boldsymbol{\tau}}\|} \tag{55}$$

where $\dot{\boldsymbol{\varepsilon}}^p$ is the rate of plastic strain tensor and $\dot{\gamma}$ is the plastic multiplier which is consistent with the loading/unloading conditions by $\dot{\gamma} \geq 0$, $\bar{\phi}^p \leq 0$ and $\dot{\gamma}\bar{\phi}^p = 0$.

In the damage stage, the loading function is given by [64,65]

$$\bar{\phi}^d\left(e^p\right) = \bar{e}^p - \kappa \tag{56}$$

with the loading/unloading conditions by $\dot{\kappa} \geq 0, \bar{\phi}^d \leq 0$ and $\dot{\kappa}\bar{\phi}^d = 0$. In this study, a simple damage law is given in Eq. (50), and the nonlocal effective plastic strain $\bar{e}^p$ [64,65] is obtained using the meshfree strain smoothing procedure [34,58] by

$$\bar{e}^p = \int_\Omega \tilde{\Psi}^c\left(\boldsymbol{X}; \boldsymbol{X}-\boldsymbol{\xi}\right) e^p d\Omega \tag{57}$$

where $\tilde{\Psi}^c$ is the strain smoothing function for regularization defined in Sect. 2. Note the strain smoothing function $\tilde{\Psi}^c$ is defined in the reference configuration and is subjected to visibility criterion described in Sect. 3 using the interactive particle enrichment algorithm. Accordingly, the rate of the nonlocal effective plastic strain $\dot{\bar{e}}^p$ is computed by

$$\dot{\bar{e}}^p = \int_\Omega \tilde{\Psi}^c\left(\boldsymbol{X}; \boldsymbol{X}-\boldsymbol{\xi}\right) \dot{e}^p d\Omega \tag{58}$$

with

$$\dot{e}^p = \sqrt{\frac{2}{3}}\dot{\gamma} \tag{59}$$

Finally, the Cauchy stress tensor $\boldsymbol{\sigma}$ for the evaluation of internal force in Eq. (31) is computed by [64,65]

$$\boldsymbol{\sigma} = \left(1 - d\left(\bar{e}^p\right)\right)\bar{\boldsymbol{\sigma}} \tag{60}$$

In this study, Eqs. (52)–(60) are utilized in the regular return mapping algorithm for explicit dynamics analysis.

References

1. Liu WK, Karpov EG, Park HS (2006) Nano mechanics and materials, theory. Multiscale methods and applications. Wiley, New York
2. Vernerey F, Liu WK, Moran B (2007) Multi-scale micromorphic theory for hierarchical materials. J Mech Phys Solids 55:2603–2651
3. Tang S, Kopacz AM, O'Keeffe SC, Olson GB, Liu WK (2013) Three-dimensional ductile fracture analysis with a hybrid multiresolution approach and microtomography. J Mech Phys Solids 61:2108–2134
4. O'Keeffe SC, Tang S, Kopacz AM, Smith J, Rowenhorst DJ, Spanos G, Liu WK, Olson GB (2015) Multiscale ductile fracture integrating tomographic characterization and 3-D simulation. Acta Mater 82:503–510
5. Chaboche JL (1988) Continuum damage mechanics. Part I: general concepts. J Appl Mech 55:59–64
6. Lemaitre J, Chaboche JL (1990) Mechanics of solid materials. Cambridge University Press, Cambridge
7. Hill R (1962) Acceleration waves in solids. J Mech Phys Solids 10:1–16
8. Lasry D, Belytschko T (1988) Localization limiters in transient problems. Int J Solids Struct 23:581–597
9. Bažant ZP, Belytschko T, Chang TP (1984) Continuum theory for strain soften. J Eng Mech 110:1666–1692
10. de Borst R, Muhlhaus HB (1992) Gradient-dependent plasticity: formulation and algorithm aspects. Int J Numer Methods Eng 35:521–539
11. Mediavilla J, Peerlings RHJ, Geers MGD (2006) A robust and consistent remeshing-transfer operator for ductile fracture simulations. Comput Struct 84:604–623
12. Wu L, Becker G, Noels L (2014) Elastic damage to crack transition in a coupled non-local implicit discontinuous Galerkin/extrinsic cohesive law framework. Comput Methods Appl Mech Eng 279:379–409
13. Geers MGD, de Borst R, Brekelmans WAM, Peerlings RHJ (1998) Strain-based transient–gradient damage model for failure analyses. Comput Methods Appl Mech Eng 160:133–153
14. Simone A, Wells G, Sluys L (2003) From continuous to discontinuous failure in a gradient-enhanced continuum damage model. Comput Methods Appl Mech Eng 192:4581–4607
15. Mazars J, Pijaudier-Cabot G (1996) From damage to fracture mechanics and conversely: a combined approach. Int J Solid Struct 33:3327–3342
16. Oliver J, Huespe AE, Pulido MDG, Chaves E (2002) From continuum mechanics to fracture mechanics: the strong discontinuity approach. Eng Fract Mech 69:113–136

17. Cazes F, Coret M, Combescure A, Gravouil A (2009) A thermodynamics method for the construction of a cohesive law from a nonlocal damage model. Int J Solids Struct 46:1476–1490
18. Oliver J (1996) Modeling strong discontinuities in solid mechanics via strain softening constitutive equations, Part I: fundamentals. Int J Numer Methods Eng 39:3575–3600
19. Moës N, Dolbow J, Belytschko T (1999) A finite element method for crack growth without remeshing. Int J Numer Methods Eng 46:131–150
20. Armero F, Linder C (2009) Numerical simulation of dynamics fracture using finite elements with embedded discontinuities. Int J Fract 160:119–141
21. Peerlings RHJ, de Borst R, Brekelmans WAM, Geers MGD (2002) Localization issues in local and nonlocal continuum approaches to fracture. Eur J Mech A/Solids 21:175–189
22. Moës N, Stolz C, Bernard PE, Chevaugeon N (2011) A level set based model for damage growth: the thick level set approach. Int J Numer Methods Eng 86:358–380
23. Tamayo-Mas E, Rodriguez-Ferran A (2014) A new continuous–discontinuous damage model: cohesive cracks via an accurate energy-transfer process. Theor Appl Fract Mech 69:90–101
24. Seabra MRR, Cesar de Sa JMA, Andrade FXC, Pires FFMA (2011) Continuous–discontinuous formulation for ductile fracture. Int J Mater Form 4:271–281
25. Broumand P, Khoei AR (2013) The extended finite element method for large deformation ductile fracture problems with a non-local damage-plasticity model. Eng Fract Mech 112–113:97–125
26. Simonsen BC, Li S (2004) Mesh-free simulation of ductile fracture. Int J Numer Methods Eng 60:1425–1450
27. Liu WK, Jun S, Zhang YF (1995) Reproducing kernel particle methods. Int J Numer Methods Fluids 20:1081–1106
28. Belytschko T, Lu YY, Gu L (1994) Element-free Galerkin methods. Int J Numer Methods Eng 37:229–256
29. Simkins DC, Li S (2006) Meshfree simulations of thermos-mechanical ductile fracture. Comput Mech 38:235–249
30. Ren B, Li S, Qian J, Zeng X (2011) Meshfree simulations of spall fracture. Comput Methods Appl Mech Eng 200:797–811
31. Ren B, Li S (2012) Modeling and simulation of large-scale ductile fracture in plates and shells. Int J Numer Methods Eng 49:2373–2393
32. Li S, Liu WK (2000) Numerical simulations of strain localization in inelastic solids using mesh-free methods. Int J Numer Methods Eng 48:1285–1309
33. Bažant ZP, Planas J (1998) Fracture and size effect in concrete and other quasibrittle materials. CRC Press, Boca Raton
34. Chen JS, Wu CT, Belytschko T (2000) Regularization of material instabilities by meshfree approximations with intrinsic length scales. Int J Numer Methods Eng 47:1303–1322
35. Chen JS, Zhang X, Belytschko T (2004) An implicit gradient model by a reproducing kernel strain regularization in strain localization problems. Comput Methods Appl Mech Eng 193:2827–2844
36. Chen JS, Wu CT, Yoon S, You T (2001) A stabilized conforming nodal integration for Galerkin meshfree methods. Int J Numer Methods Eng 50:435–466
37. Wang DD, Li Z (2013) A two-level strain smoothing regularized meshfree approach with stabilized conforming nodal integration for elastic damage analysis. Int J Damage Mech 22:440–459
38. Wu YC, Wang DD, Wu CT (2014) Three dimensional fragmentation simulation of concrete structures with a nodally regularized meshfree method. Theor Appl Fract Mech 72:89–99
39. Organ D, Fleming M, Terry T, Belytschko T (1996) Continuous meshless approximations for nonconvex bodies by diffraction and transparency. Comput Mech 18:1–11
40. Duflot M, Nguyen-Dang H (2004) A meshless method with enriched weight functions for fatigue crack growth. Int J Numer Methods Eng 59:1945–1961
41. Barbiere E, Petrinic N (2014) Three-dimensional crack propagation with distance-based discontinuous kernels in meshfree method. Comput Mech 53:325–342
42. Keysl P, Belytschko T (1999) The element-free Galerkin method for dynamic propagation of arbitrary 3-D cracks. Int J Numer Methods Eng 44:767–800
43. Fleming M, Chu YA, Moran B, Belytschko T (1997) Enriched element-free Galerkin methods for crack tip fields. Int J Numer Methods Eng 40:1483–11504
44. Rabczuk T, Belytschko T (2004) Cracking particles: a simplified meshfree method for arbitrary evolving cracks. Int J Numer Methods Eng 61:2316–2343
45. Bordas S, Rabczuk T, Zi G (2008) Three-dimension crack initiation, propagation, branching and junction in non-linear materials by an extended meshfree method without asymptotic enrichment. Eng Fract Mech 75:943–960
46. Li S, Liu WK (2004) Meshfree particle method. Springer, Berlin
47. Belytschko T, Guo Y, Liu WK, Xiao SP (2000) A unified stability analysis of meshless particle methods. Int J Numer Methods Eng 48:1359–1400
48. Beissel S, Belytschko T (1996) Nodal integration of the element-free Galerkin method. Comput Methods Appl Mech Eng 139:49–74
49. Hughes TJR, Franca LP, Hulbert GM (1989) A new finite element formulation for computational fluid dynamics: VIII. The Galerkin/least-squares method for advective-diffusive equations. Comput Methods Appl Mech Eng 73:173–189
50. Breezi F, Bristeau MO, Franca LP, Mallet M, Rogé G (1992) A relationship between stabilized finite element methods and the Galerkin method with bubble functions. Comput Methods Appl Mech Eng 96:117–129
51. Wang DD, Chen JS (2004) Locking free stabilized conforming nodal integration for meshfree Mindlin–Reissner plate formulation. Comput Methods Appl Mech Eng 193:1065–1083
52. Chen JS, Hillman M, Rüter M (2013) An arbitrary order variationally consistent integration for Galerkin Meshfree methods. Int J Numer Methods Eng 95:361–450
53. Wu CT, Koishi M, Hu W (2015) A displacement smoothing induced strain gradient stabilization for the meshfree Galerkin nodal integration method. Comput Mech 56:19–37
54. Wu CT, Wang DD, Guo Y (2016) An immersed particle modeling technique for the three-dimensional large strain simulation of particulate-reinforced metal-matrix composites. Appl Math Model 40:2500–2513
55. Wu YC, Wang DD, Wu CT (2015) A direct displacement smoothing meshfree particle formulation for impact failure modeling. Int J Impact Eng 87:169–185
56. Wu CT, Ren B (2015) A stabilized non-ordinary state-based peridynamics for the nonlocal ductile material failure analysis in metal machining process. Comput Methods Appl Mech Eng 291:197–215
57. Wu CT, Chi SW, Koishi M, Wu YC (2016) Strain gradient stabilization with dual stress points for the meshfree nodal integration method in inelastic analyses. Int J Numer Methods Eng. doi:10.1002/nme.5147 (in press)
58. Wu CT, Wu YC, Koishi M (2015) A strain-morphed nonlocal meshfree method for the regularized particle simulation of elastic-damage induced strain localization problems. Comput Mech 56:1039–1054
59. Song JH, Areias PMA, Belytschko T (2006) A method for dynamic crack and shear band propagation with phantom nodes. Int J Numer Methods Eng 67:868–893

60. Menouillard T, Belytschko T (2010) Dynamic fracture with meshfree enriched XFEM. Acta Mech 213:53–69
61. Chen JS, Pan C, Wu CT, Liu WK (1996) Reproducing kernel particle methods for large deformation analysis of non-linear structures. Comput Methods Appl Mech Eng 139:195–227
62. Wu CT, Park CK, Chen JS (2011) A generalized approximation for the meshfree analysis of solids. Int J Numer Methods Eng 85:693–722
63. Wu CT, Koishi M (2012) Three-dimensional meshfree-enriched finite element formulation for the micromechanical hyperelastic modeling of particulate rubber composites. Int J Numer Methods Eng 91:1137–1156
64. Grassl P, Jirásek M (2006) Plastic model with non-local damage applied to concrete. Int J Numer Anal Met 30:71–90
65. Unger JF, Eckardt S (2011) Multiscale modeling of concrete. Arch Comput Methods Eng 18:341–393
66. Rabczuk T, Belytschko T, Xiao SP (2004) Stable particle methods based on Lagrangian kernels. Comput Methods Appl Mech Eng 193:1035–1063
67. Belytschko T, Bindeman LP (1993) Assumed strain stabilization of the eight node hexahedral element. Comput Methods Appl Mech Eng 105:225–260
68. Park CK, Wu CT, Kan CD (2011) On the analysis of dispersion property and stable time step in meshfree method using the generalized meshfree approximation. Finite Elem Anal Des 47:683–697
69. Ju JW (1989) On energy-based coupled elastoplastic damage theories: constitutive modeling and computational aspects. Int J Solids Struct 25:803–833
70. Grassl P, Jirásek M (2006) Damage-plastic model for concrete failure. Int J Solids Struct 43:7166–7196
71. Jason J, Huerta A, Pijaudier-Cabot G, Ghavamian S (2006) An elastic plastic damage formulation for concrete: Application to elementary tests and comparison with an isotropic damage model. Comput Methods Appl Mech Eng 195:7077–7092